Rapid #: -18648802

CROSS REF ID: **6742738680005671**

LENDER: **DGU :: Lauinger Library**

BORROWER: **LT1 :: Blake Library**

TYPE:	Article CC:CCG
JOURNAL TITLE:	Gaodeng xuexiao huaxue xuebao
USER JOURNAL TITLE:	□□□□□□□□/#/□□□□□□□□ [[Kao Teng Hsueh Hsiao Hua Hsueh Hsueh Pao]]
ARTICLE TITLE:	□□□□□□□□/#/□□□□□□□□ [[Kao Teng Hsueh Hsiao Hua Hsueh Hsueh Pao]]
ARTICLE AUTHOR:	
VOLUME:	42
ISSUE:	2
MONTH:	
YEAR:	2021
PAGES:	633
ISSN:	0251-0790
OCLC #:	

Processed by RapidX: 2/14/2022 7:40:59 AM

Vol.42 高等学校化学学报 No.2
2021年2月 CHEMICAL JOURNAL OF CHINESE UNIVERSITIES 633~642

doi: 10.7503/cjcu20200711

新型石墨化氮化碳/锡/氮掺杂碳复合物的制备及储钠性能

刘志刚[1#], 李家宝[1#], 杨 剑[1], 马 浩[1], 王赪胤[1], 郭 鑫[2], 汪国秀[2]

(1. 扬州大学化学化工学院, 创新材料与能源研究院, 扬州 225002;
2. 悉尼科技大学清洁能源中心, 悉尼 2007, 澳大利亚)

摘要 钠离子电池锡负极因具有较高的理论容量(847 mA·h/g)、高电导率和合适的工作电位而备受关注. 但锡基负极材料在循环过程中会发生巨大的结构变化, 进而导致活性材料粉化失活和比容量的快速下降. 本文成功制备了基于石墨氮化碳(g-C_3N_4)、聚多巴胺衍生的氮掺杂碳(NC)和Sn纳米颗粒的复合物(g-C_3N_4/Sn/NC), 其中Sn纳米颗粒包埋在石墨氮化碳和氮掺杂碳中. 在此多层分级结构中, g-C_3N_4和NC的引入可以显著加速电子/离子的传输及电池反应动力学, 从而有助于Sn和钠离子之间的合金化反应; 此外, 这种复合结构有助于保持电极材料的结构稳定性, 进而可以获得优异的储钠性能. 作为钠离子电池负极材料, g-C_3N_4/Sn/NC在0.5 A/g电流密度下经历100次循环, 可逆容量可以达到450.7 mA·h/g; 在1.0 A/g电流密度下, 比容量为388.3 mA·h/g; 此外, 在1.0 A/g电流密度下, 经过400次循环后其比容量依旧能达到363.3 mA·h/g.

关键词 石墨氮化碳; 锡纳米颗粒; 氮掺杂碳; 储钠负极; 钠离子电池

中图分类号 O646 **文献标志码** A

Preparation of a Novel g-C_3N_4/Sn/N-doped Carbon Composite for Sodium Storage

LIU Zhigang[1#], LI Jiabao[1#], YANG Jian[1], MA Hao[1], WANG Chengyin[1*], GUO Xin[2*], WANG Guoxiu[2*]

(*1. Institute for Innovative Materials and Energy, School of Chemistry and Chemical Engineering, Yangzhou University, Yangzhou* 225002, *China*;
2. Centre for Clean Energy Technology, Faculty of Science, University of Technology Sydney, Sydney 2007, *Australia*)

Abstract Sodium-ion batteries (SIBs) based on Sn-based anodes have attracted increasing attention due to their high theoretical capacity (847 mA·h/g), high electrical conductivity and suitable operation potential. Unfortunately, the huge structural change upon cycling often causes particle pulverization and rapid capacity decay. In this work, ultrafine Sn nanoparticles with dual protection from graphitic carbon nitride (g-C_3N_4) and polydopamine derived N-doped carbon (g-C_3N_4/Sn/NC) were successfully fabricated through a designed strategy. Generally, the introduction of g-C_3N_4 and NC can dramatically accelerate the transport of electrons/ions as

收稿日期: 2020-09-24. 网络出版日期: 2020-12-28.

基金项目: 国家自然科学基金(批准号: 21375116)和江苏省优势学科资助.

联系人简介: 郭 鑫, 男, 博士, 主要从事纳米材料的调控合成及在新型二次电池中的应用研究. E-mail: xin.guo@uts.edu.au;
王赪胤, 男, 教授, 主要从事功能材料和电化学传感器研究. E-mail: wangcy@yzu.edu.cn;
汪国秀, 男, 教授, 主要从事新能源材料的开发及在能源存储与转化方面的应用研究. E-mail: Guoxiu.Wang@uts.edu.cn

共同第一作者.

well as the reaction dynamics, thus contributing to the alloying reaction between Sn and Na^+. Importantly, the ultrafine Sn as well as the dual buffering matrices can efficiently maintain the integrity of electrode upon cycling, guaranteeing the superior electrochemical performance. Benefitting from the structural advantages inherited from the ultrafine Sn nanoparticles and dual protection scaffolds, the as-obtained g-C_3N_4/Sn/NC displays excellent sodium storage performances, with high reversible capacity (450.7 mA·h/g at 0.5 A/g after 100 cycles), remarkable rate capability (388.3 mA·h/g at 1.0 A/g) and stable long-term cycling stability (363.3 mA·h/g after 400 cycles at 1.0 A/g).

Keywords g-C_3N_4; Sn nanoparticles; N-Doped carbon; Sodium-storage anode; Sodium-ion battery

1 Introduction

In order to mitigate the energy crisis and restrain environmental pollution, energy storage devices featuring high energy density, high working potential and excellent cyclability are desired. Sodium-ion batteries (SIBs), which has been considered as the most promising alternative to the market-dominated lithium-ion batteries (LIBs), have gained renewed interest due to their low-cost and high-abundance. In principle, the electrode material employed plays a significant role on the battery performance[1—3]. Compared with Li^+, the larger radius of Na^+ results in sluggish diffusion and reaction dynamics, which is unfavorable for the development of SIBs[4,5]. To meet the requirements for the next-generation rechargeable batteries, exploring novel electrode materials with high electrochemical activity and high structural stability becomes necessary[6].

Among all the available anode materials, the interest on metallic Sn-based compounds to fabricate high-performance SIBs has grown owing to their high availability, good electrical conductivity and high theoretical capacities. However, the alloying process from Sn to $Na_{15}Sn_4$ accompanies with a huge volume change of 520%, then resulting in pulverization of active materials and even loss of contact between electrode and current collector, which causes rapid capacity decay in the subsequent cycling[7]. Generally, nanostructure engineering has been proved to be an efficient approach to address the issues of Sn-based anodes. On one hand, the nanoscaled Sn can alleviate the stress induced from sodiation/desodiation by itself, ensuring structure stability. On the other hand, ultrafine Sn nanoparticles can shorten the diffusion length of Na^+, accelerating the charge transfer, which then contributes to improving the battery performance[8,9]. However, absent of carbonaceous scaffolds often leads to the aggregation of Sn nanoparticles upon cycling due to their large surface tension, showing poor electrochemical performance.

To avoid the aggregation of Sn nanoparticles and further improve the electrical conductivity and buffering ability of Sn-based electrodes, the introduction of carbonaceous agents is often adopted in previous studies[10—13]. In the designed structure containing ultrafine Sn nanoparticles and carbonaceous scaffold, the stress generated from the alloying reaction can be significantly alleviated, and meanwhile ensure the good dispersion of Sn nanoparticles in the scaffold. Besides, both the electrical conductivity and buffering ability of the composite are improved, hence contributing to the transportation of electrons/ions and integrity of electrode. As known, carbonaceous agents with nitrogen doping can remarkably modify the electronic structure and distribution of charge density, greatly increasing their electrochemical activity[14—18]. Recently, graphitic carbon nitride (g-C_3N_4), planar sheets of sp^2 hybridized carbon and nitrogen atoms, has attracted considerable attention in fields of photoelectrocatalysis and energy storage/conversion due to its layered structure, high nitrogen content, low cost and high availability[19—21]. Generally, layered g-C_3N_4 can be produced easily through thermal decomposition of urea, providing a scalable and convenient preparation approach. Besides, on account of its large surface area and superior chemical stability, previous studies have proved the feasibility

and efficiency of improving the electrochemical performances of active material after the introduction of g-C_3N_4[22—24]. However, g-C_3N_4 can only provide a robust support and short-range electron channels for individual nanoparticles in those studies, and the improvement on electrochemical performances is insufficient. In contrast, fabricating dual carbon-protected architecture, combining the advantages of short-range transportation pathways for electron and long-range conductive network, can offer convenient pathways for the charge transfer, thereby accelerating the diffusion and reaction kinetics.

Based on the considerations mentioned above, the rational combination of ultrafine Sn nanoparticles, g-C_3N_4 and conductive layer is desirable. In this work, we developed a facile strategy to prepare the target material with ultrafine Sn nanoparticles embedded in the g-C_3N_4 and polydopamine derived N-doped carbon (g-C_3N_4/Sn/NC). Such sandwich-like structure shortens the diffusion length of Na^+, accelerates the transport of electrons, maintains the integrity of electrode, and guarantees the high sodium storage activity of hybrid electrode. As a result, the obtained g-C_3N_4/Sn/NC demonstrated excellent sodium storage performances when eva-luated as anode material for SIBs. More importantly, the introduction of g-C_3N_4 and NC offers a feasible approach to obtain Sn-based anode with high performance.

2 Experimental

2.1 Apparatuses and Characterizations

Transmission electron microscopy (TEM, Tecnai 12, Philips, Netherlands), high-resolution transmission electron microscopy (HRTEM, Tecni G2F30 S-TWIN, Thermo Fisher Scientific, America), X-ray diffraction (XRD, Bruker-D8 ADVANCE, Bruker AXS, Germany), X-ray photoelectron spectroscopy (XPS, ESCALAB 250 XI, America, Thermo Scientific), *in via* confocal Raman Spectroscopy (RENISHAW, DXRxi, Thermo Fisher Scientific, America) and thermal gravimetric (TG, in air with a heating rate of 5 °C/min, Pyris 1 TGA, PerkinElmer, America) analyses were employed to conduct the material characterizations, cyclic voltammetry (CV) was performed on an Electrochemical workstation (CHI 660D, Chenhua, Shanghai) at rate of 0.1 mV/s, the electrochemical impedance spectra (EIS) tests were conducted in a frequency range of 0.1 Hz—100 kHz by setting ac amplitude at 5 mV and applied bias voltage at the open circuit voltage of the cells, respectively.

2.2 Material Syntheses

2.2.1 Preparation and Hydroxylation of g-C_3N_4

Typically, the pristine g-C_3N_4 was prepared through a facile thermal decomposition of urea at 550 ℃ for 2 h with a heating rate of 3 ℃/min in a muffle furnace. As for the hydroxylation process, 0.5 g g-C_3N_4 and 50 mL deionized water were transferred into a 100 mL autoclave and kept at 120 ℃ for 8 h, then the products were collected and washed with deionized water for several times and dried at 60 ℃ for 12h.

2.2.2 Preparation of g-C_3N_4/SnO_2

1.0 g $SnCl_4 \cdot 5H_2O$ and 100 mg hydroxylated g-C_3N_4 were dispersed in 50 mL deionized water under stirring for 2 h, then the mixture was transferred into a 100 mL autoclave and kept at 120 ℃ for 28 h. The white product was collected through centrifugation and washed with deionized water for several times, then dried at 60 ℃ overnight. Besides, pure SnO_2 was also synthesized through the same procedure without the addition of hydroxylated g-C_3N_4.

2.2.3 Preparation of g-C_3N_4/Sn/NC

The obtained 0.1 g g-C_3N_4/SnO_2 was dispersed into 100 mL of Tri-buffer solution with stirring for 30 min, then 0.2 g dopamine hydrochloride (PDA) was added into the above solution and the mixture was further stirred for another 30 min. The resultant precipitates were collected through centrifugation and washed with

deionized water for several times, and then dried overnight. The desired g-C_3N_4/Sn/NC was obtained through annealing the g-C_3N_4/SnO_2/PDA at 600 ℃ for 2 h under flowing Ar/H_2(95∶5, volume ratio). Moreover, pure Sn was prepared through annealing SnO_2 at 600 ℃ for 2 h under flowing Ar/H_2.

2.3 Electrochemical Tests

To prepare the working electrode, the active material was mixed with acetylene black and carboxymethyl cellulose in deionized water with a mass ratio of 7∶2∶1. The mass loading of active materials is about 1.0 mg/cm^2, and the specific capacity of the electrode is calculated based on the mass of the composite. The uniform slurry was then coated on a clean copper foil and dried at 100 ℃ for 12 h. The CR-2032 coin-type cells was assembled in an argon-filled glovebox with both water and oxygen contents less than 0.1 ppm. Sodium foil was used as both counter and reference electrode, and Whatman glass fiber was used as separator. The electrolyte employed was 1 mol/L $NaPF_6$ in diethylene glycol dimethylether. The sodium storage performances were tested by galvanostatic discharge/charge on NEWARE battery test system.

3 Results and Discussion

Scheme 1 typically illustrates the fabrication of desired g-C_3N_4/Sn/NC from pristine g-C_3N_4 through surface hydroxylation, *in-situ* growth of SnO_2, PDA coating, and finally thermal reduction. Firstly, the pristine g-C_3N_4 was obtained through a facile thermal decomposition of urea. Then surface hydroxylation of g-C_3N_4 was conducted to promote the *in-situ* growth of SnO_2 in the subsequent process. To further increase the electrical conductivity of the hybrid electrode and avoid the loss of Sn during the next reduction step, the g-C_3N_4/SnO_2 was further coated by PDA. Finally, after a thermal reduction performed in Ar/H_2(95∶5), the SnO_2 nanoparticles were reduced to Sn, and the PDA layers were simultaneously converted to NC. In the obtained sandwich-like structure, ultrafine Sn nanoparticles embedded in the g-C_3N_4 and NC matrices, greatly mitigating the structural change upon cycling and ensuring high sodium storage activity of the hybrid electrode, and superior sodium storage performances can be expected.

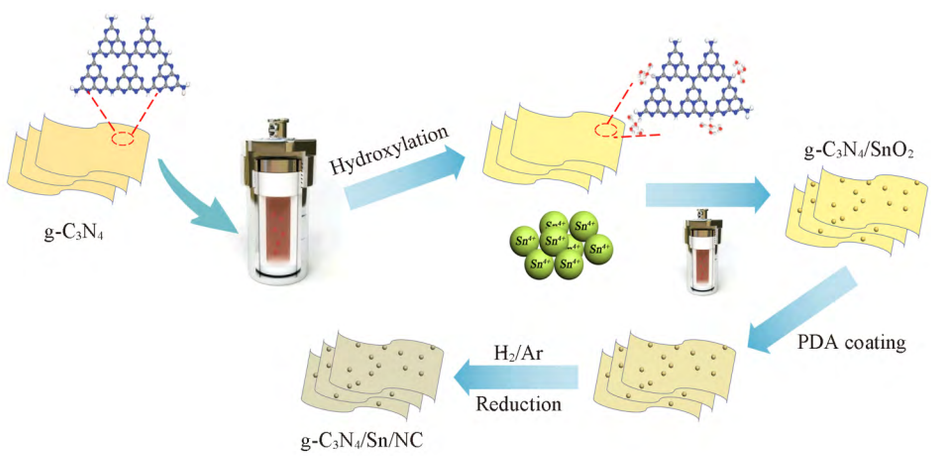

Scheme 1 Illustration of the preparation process of g-C_3N_4/Sn/NC

To detect the crystal structure of the as-prepared samples, XRD tests were performed, and the results are shown in Fig.1(A). As seen, two characteristic peaks at around 12.86° and 27.67°, corresponding to (002) and (100) planes of g-C_3N_4, respectively, can be clearly observed for g-C_3N_4[25,26]. After the *in-situ* growth of SnO_2 on the surface of g-C_3N_4, typical peaks at around 26.77°, 33.90°, 51.83° and 65.34° can be ascribed to (110), (101), (211) and (301) planes of SnO_2, respectively[27,28]. After further PDA coating and thermal reduction, the detected peaks for the g-C_3N_4/Sn/NC can be well indexed to tetragonal Sn, thus demonstrating the successfully conversion from SnO_2 to Sn. Notably, the characteristic peaks ascribed to g-C_3N_4 can hardly be

observed in the XRD patterns of g-C_3N_4/SnO_2 and g-C_3N_4/Sn/NC, which mainly results from the low contents of g-C_3N_4 in the composites. From the XPS spectrum of g-C_3N_4/Sn/NC[Fig.1(B)], elemental signals of C, N, Sn and O are presented, thereby revealing their co-existence, and the appearance of O signal should be assigned to the exposure to air. To confirm the generated NC, Raman measurement was conducted[Fig.1(C)], which displays two bands at around 1327 and 1587 cm^{-1}, resulting from the defect induced D band and graphitic carbon related G band, respectively. Additionally, the intensity ratio of D band to G band is calculated to be 0.91, hence showing a certain degree of graphitization, which can improve the electrical conductivity of the hybrid electrode[29]. Moreover, the content of Sn was determined through TG analysis in air[Fig.1(D)]. Notably, the mass loss before 530 ℃ can be assigned to the consumption of carbonaceous agents in the composite, and the increase of mass afterwards should be attributed to the oxidation of Sn with the generation of SnO_2. And similar results can be found in related studies[12,13]. Particularly, the mass fraction of Sn in the obtained composite is calculated to be 86% based on the 109.2% of the original mass maintained after the TG test. Such high content of Sn is believed to provide high capacity for the hybrid electrode.

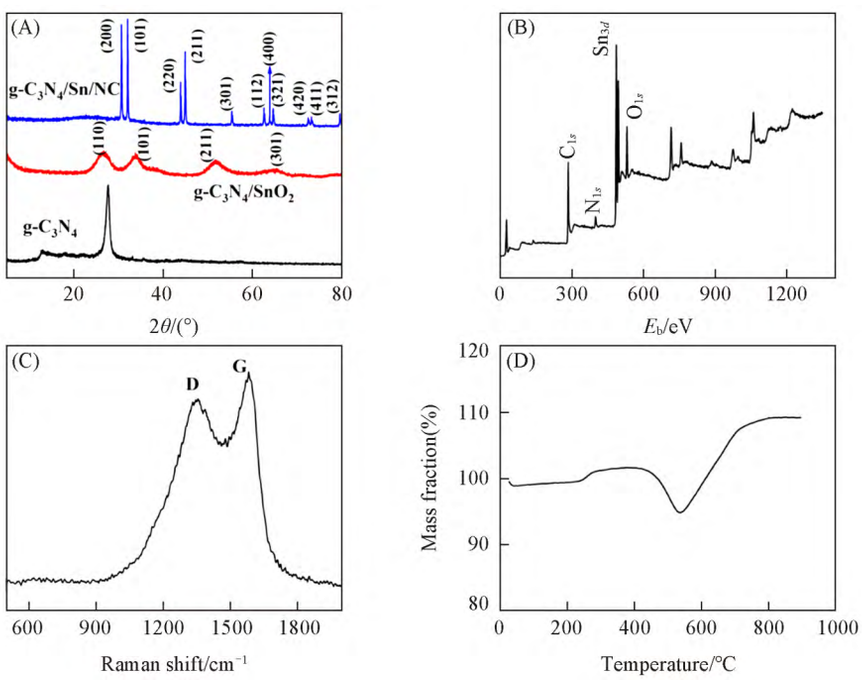

Fig. 1 Physical characterization of g-C_3N_4/Sn/NC

(A) XRD patterns of g-C_3N_4, g-C_3N_4/SnO_2 and g-C_3N_4/Sn/NC; (B) XPS spectrum of g-C_3N_4/Sn/NC; (C) Raman spectrum of g-C_3N_4/Sn/NC; (D) TG curve of g-C_3N_4/Sn/NC.

Fig.2(A) illustrates the Sn_{3d} XPS spectrum of g-C_3N_4/Sn/NC, where two peaks at around 486.9 and 495.2 eV can be detected, which correspond to $Sn_{3d_{5/2}}$ and $Sn_{3d_{3/2}}$, respectively, combining the two distinct satellite peaks(484.7 and 493.2 eV), further confirming the formation of metallic Sn in the composite[30]. As shown in Fig.2(B), four peaks at around 288.4 eV(C—C/C=C), 286.0 eV(C—N), 284.9 eV(C—O/C—O—C) and 284.1 eV(O—C=O) can be detected in the C_{1s} spectrum[31]. In the N_{1s} spectrum[Fig.2(C)], three peaks are observed at around 398.4, 400.5 and 406.5 eV, which are ascribed to pyrrolic N, pyridinic N and graphitic N, respectively. The N coordination structure is obviously different from the N_{1s} spectrum of pristine C_3N_4[Fig.2(D)], which could be attributed to the N doping in the carbon skeleton[32-34]. These characterization results comprehensively reveal the rational hybridization of g-C_3N_4, ultrafine Sn nanoparticles and NC, further confirming the feasibility of this combined approach of *in-situ* growth and subsequent thermal reduction.

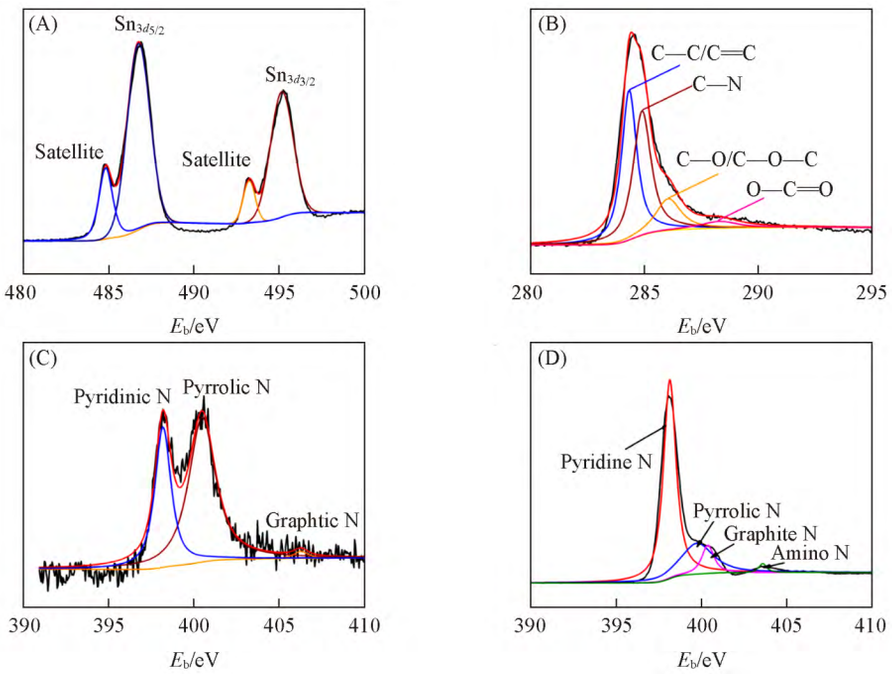

Fig. 2 XPS spectra of g-C_3N_4/Sn/NC and g-C_3N_4

(A—C) High-resolution Sn_{3d}(A), C_{1s}(B) and N_{1s}(C) spectra of g-C_3N_4/Sn/NC; (D) high-resolution N_{1s} spectra of g-C_3N_4.

The morphologies and micro-structures of as-prepared samples were characterized by TEM. As shown in Fig. 3(A) and (B), g-C_3N_4 prepared through the thermal decomposition of urea displays layered structure, thus providing a robust scaffold for the subsequent growth of SnO_2. Notably, ultrafine SnO_2 nanoparticles decorated on layered g-C_3N_4 can be clearly observed in Fig. 3(C) and (D), demonstrating the successful *in-situ*

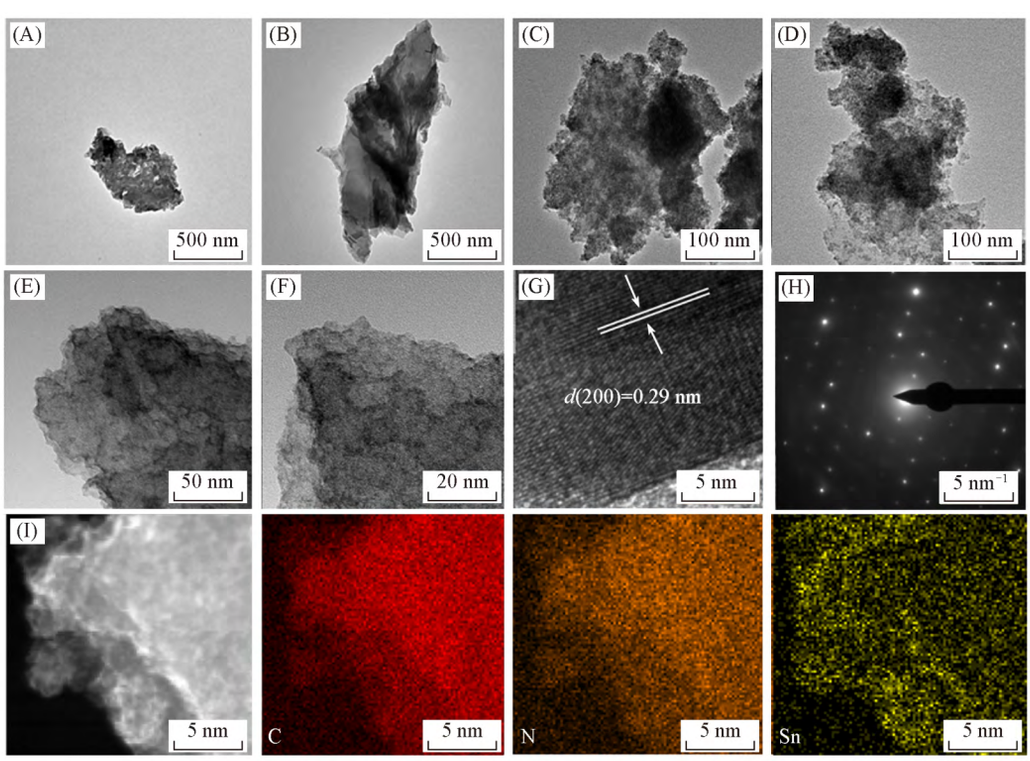

Fig. 3 TEM images of g-C_3N_4/Sn/NC, g-C_3N_4/Sn and g-C_3N_4

(A, B) TEM images of g-C_3N_4; (C, D) TEM images of g-C_3N_4/SnO_2; (E—G) HRTEM images of g-C_3N_4/Sn/NC; (H, I) SEAD pattern(H) and elemental mapping(I) of g-C_3N_4/Sn/NC.

growth. After further PDA coating and thermal reduction, the layered morphology maintains well. The dual-protected structure with Sn nanoparticles embedded in the matrices of g-C_3N_4 and NC is formed, and no aggregation can be found, thus revealing the good dispersion of Sn nanoparticles[Fig.3(E) and (F)]. Additionally, Fig.3(G) illustrates the HRTEM image of g-C_3N_4/Sn/NC, and the calculated inter-plane distance is 0.29 nm, corresponding to the (200) crystal plane of Sn. As for the selected area electron diffraction(SAED) pattern, the clear diffraction rings are assigned to the polycrystalline nature of Sn[Fig.3(H)]. Moreover, the co-existence and dispersion of C, N and Sn in the g-C_3N_4/Sn/NC composite is also confirmed by elemental mapping[Fig.3(I)], in consistent with its XPS results.

The sodium storage performances of as-synthesized samples were tested by half cells. The discharge/charge profiles of g-C_3N_4/Sn/NC in Fig.4(A) shows obvious voltage plateaus, which can be ascribed to the stepwise sodiation/desodiation of the composite. The curves are almost unchanged after 100 cycles, manifesting the stable electrode structure of g-C_3N_4/Sn/NC. Fig.4(B) displays the comparison of cycling between g-C_3N_4/Sn/NC and Sn at the current density of 0.5 A/g, and the corresponding Coulombic efficiencies are shown in Fig.4(C). Benefitting from the dual-protection of g-C_3N_4 and NC as well as the synergistic effect between them, the as-obtained g-C_3N_4/Sn/NC exhibits a better cycling performance than pure Sn, with both higher specific capacity and higher cycling stability. Specifically, reversible capacity of 450.7 mA·h/g can be received after 100 cycles for g-C_3N_4/Sn/NC electrode. In contrast, the capacity of pure Sn electrode decreases sharply during cycling, further highlighting the necessary of introduction of flexible matrix to active material with large volume change.

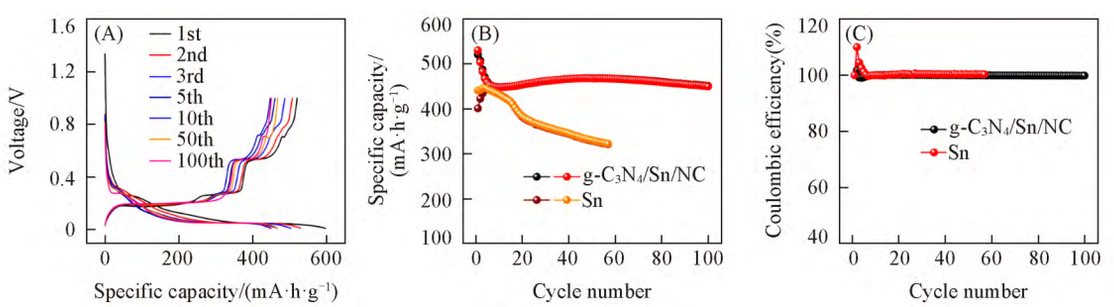

Fig. 4 Electrochemical performances of g-C_3N_4/Sn/NC at 0.5 A/g

(A) Discharge/charge profiles of g-C_3N_4/Sn/NC at 0.5 A/g; (B) cycling performances of g-C_3N_4/Sn/NC and Sn at 0.5 A/g; (C) coulombic efficiency of g-C_3N_4/Sn/NC and pure Sn electrodes at 0.5 A/g.

Fig.5(A) displays the CV curves of g-C_3N_4/Sn/NC electrode in the voltage range of 0.001—1.5 V at the scan rate of 0.1 mV/s. As illustrated, the cathodic peak at around 0.8 V appears in the first cathodic scan, which disappears in the following scans, can be denoted as the initial alloying reaction between Na^+ and Sn, the decomposition of electrolyte and generation of solid electrolyte interface(SEI) layers[35]. As for the initial anodic scan, the detected anodic peaks at around 0.23, 0.54 and 0.66 V should be assigned to the dealloying process, demonstrating that the dealloying process is a multi-step process[36]. Due to the activation of electrode and structure change after the initial cycle, both the cathodic and anodic peaks changes, which is a common phenomenon for electrode upon sodium storage. Notably, the CV curves overlap each other very well in the subsequent cycles, thus showing high reversibility of the hybrid electrode. To get more information on the charge storage kinetics of g-C_3N_4/Sn/NC and Sn electrodes, EIS measurements were performed, and the results are shown in Fig.5(B). Notably, after 50 cycles at 0.5 A/g, the semicircle of g-C_3N_4/Sn/NC electrode in the medium frequency, which is related with the charge transfer resistance(R_{ct}), is smaller than that of pure Sn electrode. This confirms the fast charge transfer kinetics in the g-C_3N_4/Sn/NC electrode, which could be the reason for the decreased polarization of the composite electrodes upon cycling. Moreover, the g-C_3N_4/Sn/NC

electrode also exhibits satisfied long-term cycling performance. As displayed in Fig.5(C), reversible capacity of 363.3 mA·h/g is remained after 400 cycles at the current density of 1.0 A/g. On the contrary, both the pure Sn and g-C_3N_4/Sn electrode display deteriorated cycling and lower specific capacity, resulting from their poor electrical conductivity and large volume change upon cycling. In principle, the excellent sodium storage performance of g-C_3N_4/Sn/NC should be attributed to its structural advantages obtained from the ultrafine Sn nanoparticles and the dual protection, improving the transportation of electrons/ions and reaction dynamics, which contributes to the increase of sodium storage performance.

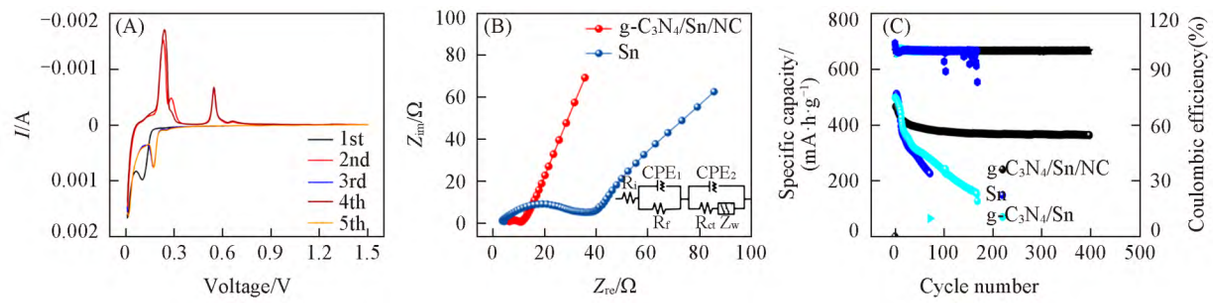

Fig. 5 CV curves of g-C_3N_4/Sn/NC at the scan rate of 0.1 mV/s in the voltage range of 0.001—1.5 V(A) and comparison of electrochemical properties of g-C_3N_4/Sn/NC and others(B, C)

(B) Nyquist plots of g-C_3N_4/Sn/NC and Sn after 50 cycles at 0.5 A/g(the inset is the equivalent circuit model); (C) long-term cycling performance of g-C_3N_4/Sn/NC, g-C_3N_4/Sn and Sn at 1.0 A/g.

Fig.6(A) presents the rate capability g-C_3N_4/Sn/NC and pure Sn anode. The as-prepared g-C_3N_4/Sn/NC electrode can display average capacities of 492.9, 455.2, 429.9, 388.3 and 174.4 mA·h/g at current densities of 0.1, 0.2, 0.5, 1.0 and 2.0 A/g, respectively. By contrast, the capacity delivered by pure Sn electrode can be neglected at rates of 1.0 and 2.0 A/g, resulting from gradual degraded inner structure and pulverization of Sn nanoparticles upon sodiation/desodiation process. In addition, the rate profiles shown in Fig.6(B) and (C) further highlight the difference of g-C_3N_4/Sn/NC and Sn on rate tests. The degraded rate profiles of pure Sn electrode should be ascribed to the pulverization of active material and even loss of electrical contact with the current collector, owing to the large volume expansion of pure Sn electrodes during cycling. As for the g-C_3N_4/Sn/NC electrode, the improved rate capability originates from the dual protection of g-C_3N_4 and NC. As seen, the voltage plateaus of g-C_3N_4/Sn/NC are maintained well, while those for pure Sn electrode degrade severely.

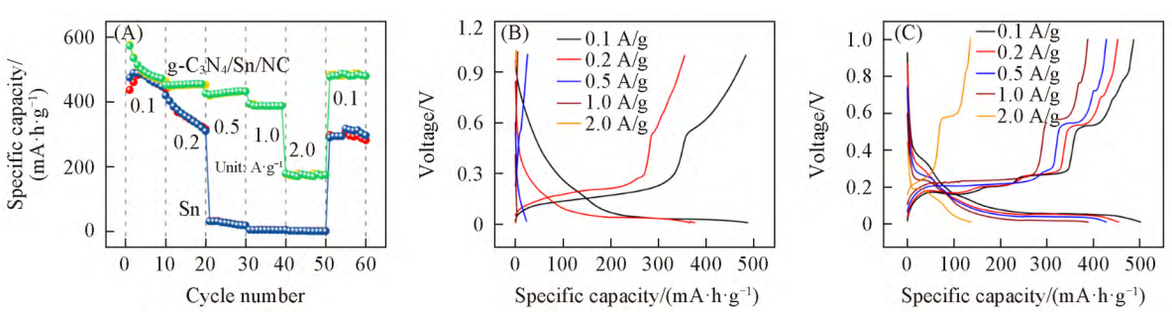

Fig. 6 Rate performance and profiles of g-C_3N_4/Sn/NC and pure Sn electrodes

(A) Rate performance of g-C_3N_4/Sn/NC and Sn; (B) rate profiles of Sn; (C) rate profiles of g-C_3N_4/Sn/NC.

As known, fabricating high conductive pathways for electrons/ions and flexible matrices can greatly decrease the polarization of electrode and mitigate the change of electrode structure, thus contributing to stable sodium storage performance. Scheme 2 schematically illustrates the origin of the excellent sodium storage performance of g-C_3N_4/Sn/NC electrode. As shown, the lack of conductive pathways among Sn particles leads to

the poor rate and cycling performance. The introduction of conductive support can indeed increase the conductivity of the hybrid electrode, and meanwhile guarantee the good dispersion of active materials. However, only short-range and in-plane conductivity are enhanced in this structure, and pulverization of Sn nanoparticles is inevitable due to the insufficient protection. After further coated with NC, the sandwich-like structure can offer both in-plane and out-plane as well as long-range conductivity, significantly increasing the charge transfer. Besides, the dual-protection from the g-C_3N_4 and NC ensures integrity of the electrode, efficiently alleviating the volume change of Sn upon electrochemical cycling, and high sodium storage activity can be guaranteed.

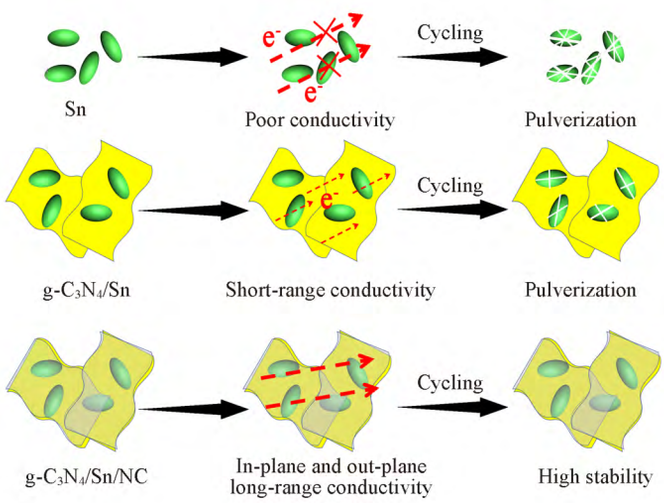

Scheme 2 Illustration of the improvement on sodium storage performance of g-C_3N_4/Sn/NC electrode

4 Conclusions

In summary, a novel g-C_3N_4/Sn/NC composite was obtained through a combined synthetic approach including *in-situ* growth, PDA coating and thermal reduction. The physical characterizations demonstrated the sandwich-like structure as well as good dispersion of Sn nanoparticles in the dual-protection matrices. As a result, the novel g-C_3N_4/Sn/NC hybrid delivered high reversible capacities of 450.7 and 363.3 mA·h/g at current densities of 0.5 A/g after 100 cycles and 1.0 A/g after 400 cycles, respectively, when evaluated as anode material for SIBs. The superior sodium storage performance should be mainly attributed to the synergistic effects between Sn nanoparticles, g-C_3N_4 and NC, where g-C_3N_4 layers offer *in-situ* growth sites for the good dispersion of Sn nanoparticles, and meanwhile the NC can guarantee high conductivity and integrity of electrode. Additionally, this study provides an efficient strategy to fabricate alloy-based electrodes for high-performance SIBs.

This work is supported by the National Natural Science Foundation of China (No. 21375116) and the Priority Academic Program Development of Jiangsu Higher Education Institutions, China.

References

[1] Wang Z., Liu S., Hou Q., Zhang L., Zhang A., Li F., Zhang X., Wu P., Zhu X., Wei S., Zhou Y., *J. Alloys Compd.*, **2020**, *840*, 155703
[2] Li J., Yan D., Lu T., Yao Y., Pan L., *Chem. Eng. J.*, **2017**, *325*, 14—24
[3] Du Y., Ma W., Li H., *Small*, **2020**, *16*(11), e1907468

[4] Yang Z., Zhang J., Kintner-Meyer. M. C., Lu X., Choi. D., Lemmon. J. P., Liu. J., *Chem. Rev.*, **2011**, *111*(5), 3577
[5] Li S., Zhao Z., Li C., Liu Z., Li D., *Nano-Micro Lett.*, **2019**, *11*(1), 14
[6] Ma D., Li Y., Mi H., Luo S., Zhang P., Lin Z., Li J., Zhang H., *Angew. Chem. Int. Ed. Engl.*, **2018**, *57*(29), 8901—8905
[7] Mao M., Yan F., Cui C., Ma J., Zhang M., Wang T., Wang. C., *Nano Lett.*, **2017**, *17*(6), 3830—3836
[8] Jiang Y., Wang Y., Jiang J., Liu S., Li W., Huang S., Chen Z., Zhao B., *Electrochim. Acta*, **2019**, *312*, 263—271
[9] Yue L., Jayapal M., Cheng X., Zhang T., Chen J., Ma X., Dai X., Lu H., Guan R., Zhang.W., *Appl. Surf. Sci.*, **2020**, *512*, 145686
[10] Luo X., Huang J., Li J., Cao L., Cheng Y.,Guo L., Wang Y., Qi H., *Appl. Surf. Sci.*, **2019**, *491*, 95—104
[11] Wang Z., Dong K., Wang D., Chen F., Luo S., Liu Y., He C., Shi C., Zhao N., *Chem. Eng. J.*, **2019**, *371*, 356—365
[12] Li Y., Ou C., Zhu J., Liu Z., Yu J., Li W., Zhang H., Zhang Q., Gu Z., *Nano Lett.*, **2020**, *20*(3), 2034—2046
[13] Cheng D., Yang L., Hu R., Liu J., Che R., Cui J., Wu Y., Chen W., Huang J., Zhu M., Zhao. Y. J., *ACS Appl. Mater & Interfaces.*, **2019**, *11*(40), 36685—36696
[14] Li L., Zhao J., Zhu Y., Pan X., Wang H., Xu J., *Electrochim. Acta*, **2020**, *353*, 136532
[15] Song X., Li X., Chen Z., Wang Z., *Materials Lett.*, **2020**, *275*, 128109
[16] Zhang S., Mi J., Zhao H., Ma W., Dang L., Yue L., *J. Alloys Compd.*, **2020**, *842*, 155642
[17] Li J., Yan D., Hou S., Lu T., Yao.Y., Pan L., *Chem. Eng. J.*, **2018**, *354*, 172—181
[18] Li J., Li J., Ding Z., Zhang X., Li Y., Lu T., Yao Y., Mai W., Pan L., *Chem. Eng. J.*, **2019**, *378*, 122108
[19] Li G., Lian Z., Wang W., Zhang D., Li H., *Nano Energy*, **2016**, *19*, 446—454
[20] Yuan M., Teng Z., Wang S., Xu Y., Wu P., Zhu Y., Wang C., Wang G., *Chem. Eng. J.*, **2020**, *391*, 123506
[21] Hankel. M., Ye D., Wang L., Searles D. J., *J. Phys. Chem. C*, **2015**, *119*(38), 21921—21927
[22] Hou Y., Li J., Wen Z., Cui S., Yuan C., Chen J., *Nano Energy*, **2014**, *8*, 157
[23] Shi M., Wu T., Song X., Liu J., Zhao L., Zhang P., Gao L., *J. Mater. Chem. A.*, **2016**, *4*(27), 10666—10672
[24] Weng G. M., Xie Y., Wang H., Karpovich C., Lipton J., Zhu J., Kong J., Pfefferle L. D., Taylor A. D., *Angew. Chem. Int. Ed. Engl.*, **2019**, *58*(39), 13727—13733
[25] Niu P., Zhang L., Liu G., Cheng. H. M., *Adv. Funct. Mater.*, **2012**, *22*(22), 4763—4770
[26] Zang Y., Li L., Li X., Lin R., Li G., *Chem. Eng. J.*, **2014**, *246*, 277—286
[27] He Y., Zhang L., Fan M., Wang X., Walbridge. M. L., Nong Q., Wu Y., Zhao L., *Sol. Energy Mater. Sol. Cells.*, **2015**, *137*, 175—184
[28] Chen X., Zhou B., Yang S., Wu H., Wu Y., Wu L., Pan J., Xiong X., *RSC Adv.*, **2015**, *5*(84), 68953—68963
[29] Xie X., Kretschmer K., Zhang J., Sun B., Su D., Wang G., *Nano Energy*, **2015**, *13*, 208—217
[30] Wu X., Qian C., Wu H., Xu L., Bu L., Piao Y.,Diao G., Che M., *Chem. Commun.*, **2020**, *56*(55), 7629—7632
[31] Wang Y., Tao L., Chen R., Li H., Su H., Zhang N., Liu Q., Wang S., *Chem. Res. Chinese Universities*, **2020**, *36*(3), 453—458
[32] Ye X., Lin Z., Liang S., Huang X., Qiu X., Qiu Y., Liu X., Xie D., Deng H., Xiong. X., Lin Z., *Nano Lett.*, **2019**, *19*(3), 1860—1866
[33] Tang H., Xiang M., Xu B., Li Y., Han W., Liu Z., *Chem. Res. Chinese Universities*, **2018**, *34*(6), 1004—1008
[34] Luo L., Song J., Song L., Zhang H., Bi Y., Liu L., Yin L., Wang F., Wang G., *Nano-Micro Lett.*, **2019**, *11*(1), 63
[35] Chen S., Ao Z., Sun B., Xie X., Wang G., *Energy Storage Mater.*, **2016**, *5*, 180—190
[36] Liu M., Huang J., Li J., Cao L., Zhao Y., Ma M., Koji K., *J. Alloys Compd.*, **2020**, *834*, 155177

(Ed.: W, K, M)